



High-density accessible Ru—O—Co moieties with accelerated formation of activated oxygen species for freshwater and seawater electrolysis

Deqiang Kong^a, Chao Meng^{a,*}, Yanmin Wang^b, Xuemin Chen^c, Jialin Zhang^a, Lei Zhao^b, Jianglong Ji^b, Liang Zhang^b, Yue Zhou^{a,b,**}

^a College of Electrical Engineering and Automation, Shandong University of Science and Technology, Qingdao 266590, China

^b College of Energy Storage Technology, Shandong University of Science and Technology, Qingdao 266590, China

^c College of Science, Hebei University of Science and Technology, Shijiazhuang 050018, China

ARTICLE INFO

Keywords:

High-density accessibility
Ru₃O₃Co moieties
Activated oxygen species
Alkaline water splitting
AEM flow electrolyzer

ABSTRACT

Promoting the activated oxygen formation and the accessible site density is crucial for boosting the mass and price activity of Ru in water/seawater electrolysis. However, a rational catalyst architecture is lacking to satisfy the above requirements. Herein, Ru was intentionally embedded into few-layer Co₃O₄ (Ru-Co₃O₄) to construct high-density accessible Ru—O—Co moieties for water/seawater splitting. The moiety structure accelerates the generation and dissociation of activated H₂O during hydrogen evolution reaction (HER), and ensures the rapid evolution of key “activated oxygen” species in oxygen evolution reaction (OER), thus improving HER/OER intrinsic kinetics. Besides, these moieties embedded within few-layer structure effectively promote site formation and utilization. Consequently, compared with Ru/C and Pt/C, an order of magnitude increase in mass and price activity was achieved for bifunctional HER/OER. When applied in an anion-exchange-membrane (AEM) electrolyzer, this catalyst realizes industrial-level current densities for freshwater and seawater electrolysis, more than twice than Ru/C⁽⁺⁾||Pt/C⁽⁻⁾, and robust durability.

1. Introduction

Green electricity-driven alkaline water splitting, especially AEM water electrolysis, is a promising and scalable approach for producing hydrogen [1–4]. Despite its potential, the overall efficiency of hydrogen production is limited by the complex adsorption, dissociation, and desorption of various reaction species involved in both cathodic HER and anodic OER, as well as multi-electron transfer [5–8]. While Pt/C and Ir/C are considered benchmark electrocatalysts for promoting the HER and OER, respectively, there is a pressing need to discover effective and economical bifunctional alternatives that can reduce the cost and simplify the device [9,10]. Ru, as the cheapest Pt-group metal, is a desirable candidate for efficiently catalyzing both HER and OER [11]. For the HER side, the hydrogen binding strength of Ru (65 Kcal mol⁻¹) is similar as that of the state-of-the-art Pt (62 Kcal mol⁻¹), suggesting its feasible H adsorption and H₂ desorption [12]. For the OER side, Ru exhibits comparable catalytic activity to Ir [13]. However, the ability of Ru to adsorb and activate the reactant H₂O molecules is too weak to

obtain sufficient dissociated H* for subsequent hydrogen evolution [14]. Moreover, Ru is located on the weak adsorption side of the OER volcano plot, meaning that the sluggish generation of active oxygen-containing intermediates hinders it to achieve the summit activity [15]. Therefore, accelerating the formation of activated oxygen species is critical to enhancing the bifunctional intrinsic activity of Ru catalyst for alkaline HER and OER. Further considering the cost of the catalyst, it is essential to reduce the dosage of Ru by promoting site utilization, ultimately improving the mass activity and price activity.

To enable Ru to meet the aforementioned requirements, cheap transition metals (M) have been introduced to create a variety of bi- or multi-metallic catalysts, including M@Ru core-shell, Ru-M alloys, and Ru—O—M moieties [16–19]. Among these, the construction of Ru—O—M moieties through combining metal oxides or hydroxides with Ru has gained much attention. On the one hand, Ru—O—M moieties can modulate the electronic structure of metal catalytic centers to optimize the adsorption or formation of oxygen-containing reactants/intermediates, thereby realizing the improvement of intrinsic

* Corresponding author.

** Corresponding author at: College of Electrical Engineering and Automation, Shandong University of Science and Technology, Qingdao 266590, China.

E-mail addresses: ChaoMeng@sdust.edu.cn (C. Meng), zhouyue@sdust.edu.cn (Y. Zhou).

catalytic activity [14]. On the other hand, Ni, Co, Mo, Cu, and other metal (hydr)oxides possess several advantages such as abundant sources, low cost, as well as excellent chemical and electrochemical stabilities [20–23]. For instance, Liu et al. synthesized Ru/MoO₂ composite nanoparticles with Ru—O—Mo interfaces for alkaline HER catalysis [14]. The Ru—O—Mo interfaces exhibited tenfold stronger H₂O adsorption ability and significantly reduced the HER overpotential compared to the pure Ru catalyst. Besides, the Ru catalysts were loaded on CeO₂ nanorods for low-temperature CO oxidation [24]. The formed Ru—O—Ce structure at the interface promotes the adsorption/dissociation of oxygen, eventually achieving a superior CO conversion of ~9% at room temperature.

Given the geometric advantage of two-dimensional (2D) materials with a large surface area, loading Ru onto 2D metal oxide/hydroxide supports has been reported to increase interfacial Ru—O—M moieties [25]. Very recently, Kong's group successfully prepared CuO nanosheets-supported Ru nanocrystals with active Ru—O—Cu moieties at the interface [26]. These moieties efficiently facilitate water adsorption and dissociation via reinforcing surface oxophilicity, accordingly expediting the reaction kinetics and enhancing the intrinsic HER activity. Moreover, the increase in the number of active moieties contributed to high apparent activity. While the above advances have obtained Ru—O—M moieties with improved intrinsic catalytic activity, it is worth noting that the content of Ru in either composite nanoparticle catalysts or supported catalysts is usually very high, some even reaching 30 wt% [14,26]. This is because the catalytically active Ru—O—M moieties can only exist at the interface of these catalysts, which is not conducive to the formation and utilization of catalytic moieties [26]. So only by increasing the Ru content can more Ru—O—M be guaranteed, and eventually better apparent catalytic performance is realized. However, when the Ru content exceeds a certain level, such as 9% in the reported Ru-WO₃ catalyst, the apparent activity does not increase as fast as the number of interfacial Ru—O—M moieties, which leads to a decline in mass activity and price activity [27,28]. Therefore, under the premise of fixed Ru content, how to maximize the formation and exposure of Ru—O—M moieties is crucial to improve the mass and price activity, so as to achieve the full utilization of Ru. A potential solution is to construct the embedded Ru—O—M in the 2D few-layer structure, which is expected to boost the density and accessibility of active moieties. Besides, considering the advantages of Co₃O₄ with a strong interaction with H₂O in HER and good activity in OER, the Ru—O—Co embedded within few-layer structure, which can be created via doping Ru into Co₃O₄ nanosheets, may boost the bifunctional HER/OER catalysis [29,30]. Recently, some works reported the Ru-doped Co₃O₄ nanorods and nanofibers for improved alkaline HER or OER, and found that the doped Ru can regulate the electronic structure of Co single active centers to enhance the adsorption of reactant OH[−] in OER [31–33]. Nevertheless, it is rarely reported the embedded Ru—O—Co in the 2D few-layer structure for bifunctional water splitting in alkaline medium. In view of the fact that the active moieties often bring unexpected synergistic catalytic effects compared to the single sites [34,35], it is necessary and challengeable to systematically investigate the bifunctional HER/OER catalytic behavior of the above advanced Ru—O—Co architecture and uncover the underlying performance enhancement mechanism.

Herein, we constructed high-density accessible Ru—O—Co moieties via embedding Ru into the few-layer Co₃O₄ nanosheets, namely Ru-Co₃O₄. This catalyst with the Ru content of about 7.01% exhibits impressive HER/OER bifunctional performance, especially the mass activity and price activity. The HER mass activity (6.82 A mg^{−1}) and price activity (456.19 A dollar^{−1}) of Ru-Co₃O₄ are more than one order of magnitude higher than those of Ru/C and Pt/C, while its OER mass activity (1.87 A mg^{−1}) and price activity (125.08 A dollar^{−1}) are about 21.3 times than those of Ru/C. The excellent mass and price activity of Ru-Co₃O₄ are attributed to the increased intrinsic activity and high density of accessible Ru—O—Co moieties. Compared with references Ru/C and Co₃O₄, the embedded Ru—O—Co in the few-layer structure

strengthens the adsorption and activation of reactant H₂O molecules in HER, and also accelerates the generation of key “activated oxygen” species during the OER, thus markedly improving the reaction kinetics and intrinsic HER/OER bifunctional activities. Besides, the above-advanced catalyst structure benefits the formation and utilization of active sites, with the increased accessible site density in contrast to the interfacial Ru—O—Co in Ru-loaded Co₃O₄ (Ru@Co₃O₄). Further, when coupled in a practical AEM electrolyzer, the Ru-Co₃O₄ delivers industrial-level current densities of 1 A cm^{−2} at 2.03 V for water splitting and 0.41 A cm^{−2} at 1.71 V for seawater splitting, both of which are more than twice than those of the assembly of Ru/C and Pt/C, as well as robust durability over 48 h. This work clearly demonstrates the importance of the catalyst structure design for boosting the mass activity and price activity of Ru catalyst in water/seawater electrolysis.

2. Experimental section

2.1. Chemicals and reagents

Cobalt chloride (CoCl₂·6 H₂O) and ruthenium chloride (RuCl₃·H₂O) were purchased from Shanghai Aladdin Reagent Co., Ltd. Sodium hydroxide (NaOH), sodium borohydride (NaBH₄), and absolute ethanol were obtained from Sinopharm Chemical Reagent Co., Ltd. Carbon fiber paper (CFP, HCP020N, 210 *200 *0.2 mm), Nafion solution (5.0 wt%, Dupont), commercial Ru/C (20.0 wt%) and commercial Pt/C (40.0 wt%) were acquired from Shanghai Hesin Electric Co., Ltd. All reagents are used as received without further purification.

2.2. Preparation of Ru-Co₃O₄, Ru@Co₃O₄, and Co₃O₄ catalysts

In a typical experiment, 1.25 mmol CoCl₂·6 H₂O, 0.625 mmol RuCl₃·H₂O, and 0.1 mol NaOH were dissolved in 15 mL of deionized water and stirred vigorously for 2 h. After that, the uniform mixture was transferred to a 25 mL stainless steel autoclave lined with polytetrafluoroethylene and placed in an oven at 130 °C for 12 h. The obtained precursor was washed several times with deionized water and ethanol, and then placed in a freeze-dryer until it was completely lyophilized. Finally, the dried precursor was annealed at 400 °C in an argon atmosphere for 2 h to obtain the Ru-Co₃O₄. Besides for the preparation of Co₃O₄, the synthesis procedure is similar except without the addition of RuCl₃·H₂O.

For the preparation of Ru@Co₃O₄, a simple chemical reduction method was employed using RuCl₃·H₂O as the Ru precursor and NaBH₄ as the reductant. Firstly, a 0.3 mM Ru precursor solution was prepared by dispersing RuCl₃·H₂O in 1/1 (v/v) aqueous ethanol. Next, 0.1 M NaBH₄ was added to the Ru precursor solution and vigorously stirred. Afterward, Co₃O₄ nanosheet powders were fully immersed in the above solution for 5 h. The resulting product was cleaned, dried, and annealed at 300 °C in an Ar atmosphere for 2 h to obtain the Ru@Co₃O₄.

2.3. Material characterizations

Powder X-ray diffraction (XRD) was performed on a Bruker D8 Advance diffractometer at 40 kV and 40 mA using Cu K α radiation (λ = 0.15406 nm). Transmission electron microscopy (TEM), high-resolution TEM (HRTEM), and high-angle annular dark-field scanning transmission electron microscopy (HAADF-STEM) images were obtained with a FEI Talos 200 S high-resolution transmission electron microscope at an acceleration voltage of 200 kV. Raman spectra were obtained by a DXR2 Raman Microscope (Thermo Fisher) with 532 nm line of Ar⁺ laser as the excitation source. X-ray photoelectron spectrum (XPS) analysis was performed on a PHI 5000 VersaProbe system using monochromatic Al K α radiation (1486.6 eV). Fourier transform infrared spectrum (FTIR) measurements were conducted on a Thermo Fisher iS50 instrument. For the H₂O adsorption test of FTIR, the samples were exposed to water vapor and the infrared spectra were collected from the wet samples. The

background signal was established using the infrared spectrum of pure water, with a wavenumber range of 2000–4000 cm^{-1} .

2.4. Three-electrode electrochemical measurements

The HER and OER measurements were performed on a typical three-electrode system using a CHI 760E electrochemical working station (Shanghai, Chenhua Co., China). Here, the working electrode was prepared by coating the catalyst on CFP with a loading mass of 0.3 mg cm^{-2} . In detail, 5 mg of catalyst was dispersed in the mixture of ethanol (665 μL), deionized water (335 μL), and Nafion solution (20 μL). The above mixture was then ultrasonically treated for 30 min to obtain the catalyst ink, which was finally loaded on the CFP support. Prior to HER and OER measurements, Ar and O_2 were pumped into a 1 M KOH electrolyte for at least 30 min respectively to achieve saturation. The linear sweep voltammetry (LSV) curves were recorded at a scan rate of 5 mV s^{-1} and the potentials were referenced to the RHE using Eq. 1:

$$E_{\text{RHE}} = E_{\text{SCE}} + 0.0591 \text{ pH} + 0.242 \quad (1)$$

The mass activities (MA) of Ru- Co_3O_4 , Ru@ Co_3O_4 , Ru/C, and Pt/C were calculated according to Eq. 2, where J is the current density, and m is the mass loading of Ru/Pt.

$$\text{MA (A mg}^{-1}\text{)} = J \text{ (mA cm}^{-2}\text{)} / m \text{ (}\mu\text{g cm}^{-2}\text{)} \quad (2)$$

For easy to compare, the mass activity values of the above catalysts were normalized to Ru or Pt price through Eq. 3 to obtain their price activities (PA).

$$\text{PA (A dollar}^{-1}\text{)} = \text{MA (A mg}^{-1}\text{)} / \text{price (dollar g}^{-1}\text{)} \quad (3)$$

Moreover, the electrochemical impedance spectroscopy (EIS) was tested in the frequency range of 0.1 Hz–100 kHz, and the I-t test was carried out at a constant current density of 100 mA cm^{-2} .

2.5. The determination of electrochemical double-layer capacitance (C_{dl}) and turnover frequency (TOF)

The electrochemical C_{dl} of HER and OER was tested using cyclic voltammetry (CV). The scan rate was set to 20, 40, 60, 80, 100, and 120 mV s^{-1} , and the voltage range was selected at 0.18–0.23 V for HER and 1.18–1.23 V for OER.

The TOF value was calculated according to Eq. 4, where J (mA cm^{-2}) stands for the current density at a given potential, S (cm^2) is the surface area of the electrode, n is the number of electrons that are consumed to produce one H_2 or O_2 molecules (2 for HER and 4 for OER), F is the Faraday constant (96485 C mol^{-1}), and m (mol) represents the quantity of active sites.

$$\text{TOF} = (J \times S) / (n \times F \times m) \quad (4)$$

2.6. AEM water electrolyzer test

An AEM flow electrolyzer that couples the HER with OER was assembled to demonstrate hydrogen production at commercially relevant levels. The Ru- Co_3O_4 loaded on CFP was directly used for both the cathode and anode with an effective area of 1 cm^2 , and FAA-3-50 (Fumatech, Germany) was used as the AEM. For freshwater electrolysis, the flow chamber was circulated with 1 M KOH solution under a flow rate of 5 mL min^{-1} , while for seawater electrolysis, the electrolyte was changed with the mixed solution (1 M KOH+0.5 M NaCl+0.1 M Na_2SO_4). The extra addition of SO_4^{2-} has been reported to repel Cl^- , which is beneficial to improve the corrosion resistance of the catalyst in the process of seawater electrolysis. The electrochemical data for the flow-electrolyzer was measured at 70 $^\circ\text{C}$ using a Metrohm Autolab workstation (PGSTAT302N).

2.7. Calculation of basic electricity expense for H_2 production [36]

The total electricity consumption for H_2 production was calculated according to the following equation:

$$W = I \times \int U \, dt \quad (5)$$

Where the W is the total electricity consumption, I is the electrolyzer current, U is the electrolyzer voltage, and t is the reaction time.

The amount of H_2 generation was calculated based on the following equation:

$$V = 22.4 \times I \times t / (Z \times F) \quad (6)$$

Where V is the volume of produced H_2 , Z is the electron transfer number (the value of 2 for HER), and F is the Faraday constant (96485 C mol^{-1}).

According to the above results, the basic electricity expense for H_2 production was calculated as:

$$Q = W / V \text{ (kWh m}^{-3} \text{H}_2\text{)} \quad (7)$$

For an ideal catalyst, assuming that it has no performance decay during the stability test of water splitting, the calculation of basic electricity expense for H_2 production can be simplified to the formula [$Q = 2.39 \times U \text{ (kWh m}^{-3} \text{H}_2\text{)}$] according to the Eqs. (5–7).

2.8. Density functional theory (DFT) calculations

We have employed the Vienna Ab initio Simulation Package (VASP) to perform all DFT calculations [37]. The elemental core and valence electrons were represented by the projector augmented wave (PAW) method and plane-wave basis functions with a cutoff energy of 400 eV. Generalized gradient approximation with the Perdew-Burke-Ernzerh of (GGA-PBE) exchange-correlation functional was employed in all the calculations [38]. Geometry optimizations were performed with the force convergency smaller than 0.05 eV/Å. Half atoms at bottom of Ru (001) surface and 28 atoms at bottom of $\text{Co}_3\text{O}_4(111)$ surface were fixed in all the calculations. Monkhorst-Pack k-points of $4 \times 4 \times 1$ and $2 \times 2 \times 1$ were applied for all the calculations of Ru(001) and $\text{Co}_3\text{O}_4(111)$, respectively. Ru/ $\text{Co}_3\text{O}_4(111)$ is one Ru atom doping the Co atoms on the $\text{Co}_3\text{O}_4(111)$ surface. The Gibbs free energy (ΔG) for each electrochemical process is calculated as:

$$\Delta G = \Delta E + \Delta E_{\text{ZPE}} - T\Delta S \quad (8)$$

Where the value of ΔE , ΔE_{ZPE} and ΔS denotes the changes of DFT energy, the zero-point energy and the entropy at 300 K, respectively.

3. Results and discussion

3.1. Synthesis and characterization of high-density accessible Ru—O—Co moieties

The synthetic route of Ru- Co_3O_4 with high-density accessible Ru—O—Co moieties is schematically depicted in Fig. 1a. We first synthesized the Ru-Co precursor via a hydrothermal method, which was subsequently annealed in Ar flow to obtain the Ru- Co_3O_4 with Ru—O—Co moieties. For comparison, the Co_3O_4 was prepared in a similar procedure except no addition of Ru source (Fig. S1). TEM and scanning electron microscope (SEM) were adopted to observe the material morphology. As shown in Fig. 1d and S2a, the Ru- Co_3O_4 exhibits the morphology of nanosheets with an average thickness of about 7 nm (Fig. 1h). The few-layer nanosheet structure is favourable for rapid mass transfer and high accessibility of active sites [39]. Fig. 1b displays the XRD pattern of Ru- Co_3O_4 . Except for a small amount of CoO phase, other diffraction peaks correspond well with the standard PDF card of cubic Co_3O_4 (JCPDS 43–1003). Notably, all diffraction peaks of Ru- Co_3O_4 shift towards a lower diffraction angle by about 0.1° compared with the

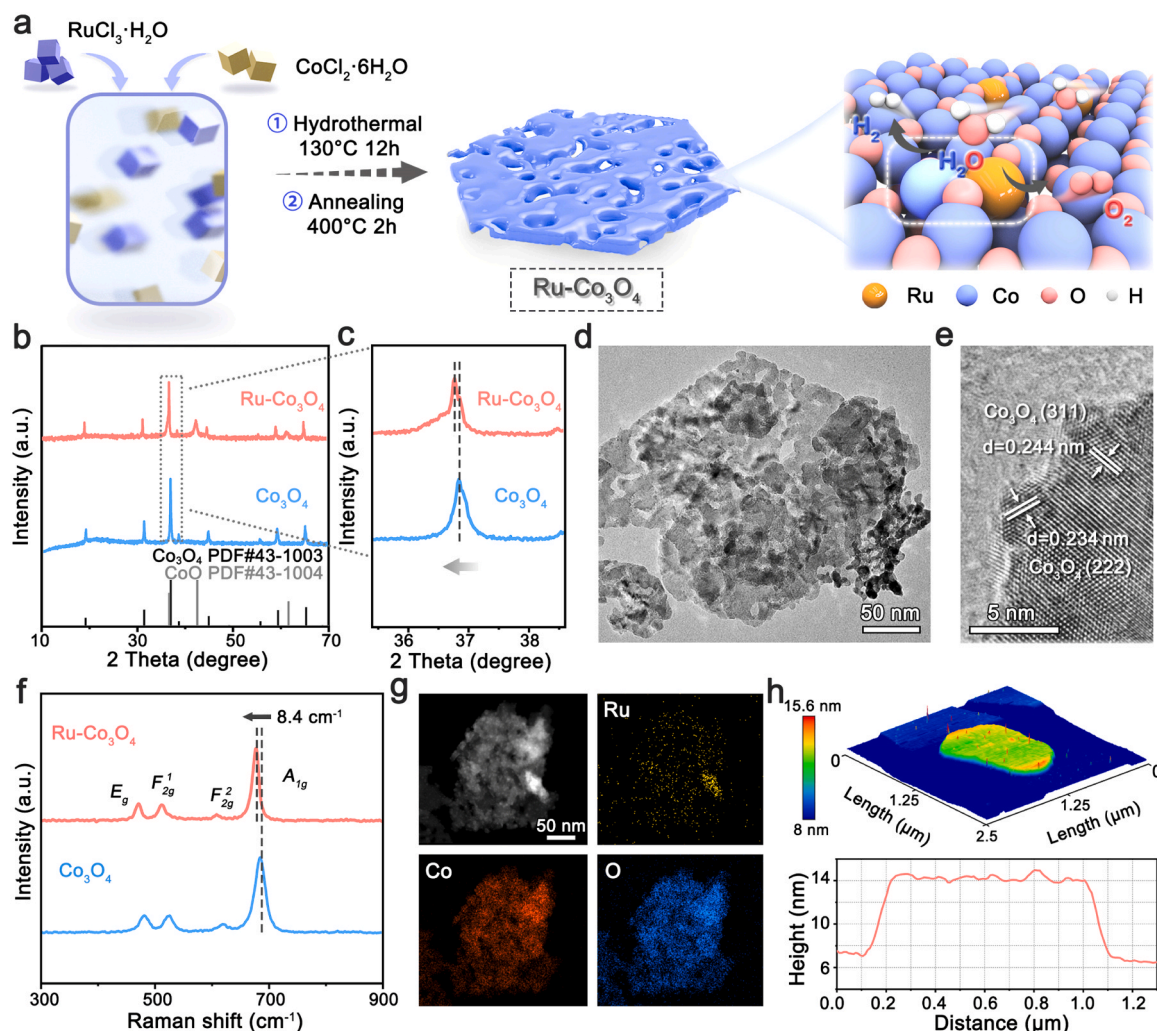


Fig. 1. (a) Schematic illustration of the synthetic procedures of Ru-Co₃O₄ with Ru—O—Co moieties. (b) XRD patterns and (c) corresponding local magnification of Ru-Co₃O₄ and Co₃O₄. (d) Low-magnification TEM and (e) HRTEM images of Ru-Co₃O₄ nanosheet. (f) Raman spectra of Ru-Co₃O₄ and Co₃O₄. (g) HAADF-STEM image and corresponding EDS mappings of Ru-Co₃O₄. (h) Atomic force microscopy image of Ru-Co₃O₄ nanosheets with the thickness of about 7 nm.

Co₃O₄ reference and no Ru-related peaks appear, indicating that Ru may be doped into the lattice of cobalt oxides, which is confirmed by the EDS spectra (Fig. 1c and S2b). The lattice arrangement was investigated by HRTEM, where the Ru-Co₃O₄ presents a slightly expanded spacing of (311) and (222) crystal planes due to the bigger size of doped Ru atom than that of Co atom (Fig. 1e). The above results were also demonstrated by the Raman spectra (Fig. 1f). Four Raman peaks at 471, 513, 609, and 678 cm⁻¹ can be observed, corresponding to the E_g, F_{2g}¹, F_{2g}², and A_{1g} vibrational modes of spinel Co₃O₄, respectively [40–42]. Noteworthy, the peak positions of Ru-Co₃O₄ have an obvious shift to lower wavenumbers in contrast to the reference Co₃O₄, caused by the Ru-doping-induced lattice expansion. The EDS mappings of Ru-Co₃O₄ manifest that the doped Ru is uniformly distributed in Co₃O₄ nanosheets (Fig. 1g), and the doping concentration is determined to be 7.01 wt% via ICP-MS (Table S1).

XPS was conducted to probe the surface chemical states and electronic environment of catalysts. From the XPS survey full spectrum, it can be found that the Ru-Co₃O₄ is composed of Ru, Co, and O elements (Fig. S3). Fig. 2a presents the Ru 3p XPS spectra of Ru-Co₃O₄ and Ru/C. In comparison with the Ru/C which has a pair of peaks corresponding to Ru⁰ 3p_{3/2} (461.9 eV) and Ru⁰ 3p_{1/2} (484.3 eV), the peak positions of Ru-Co₃O₄ shift by about 0.3 eV towards the direction of RuO₂ (462.8 and 485.8 eV) and RuO₂ (464.2 and 487.2 eV), revealing that the Ru is doped into Co₃O₄ in a mixed valence of 0 and +2 [43]. Besides, the Co

2p XPS spectra of Ru-Co₃O₄ and Co₃O₄ are shown in Fig. 2b, where two sets of sharp peaks locate at 781.4/796.3 eV and 779.6/794.8 eV, belonging to Co²⁺ and Co³⁺, respectively, accompanied by two weak satellite peaks at 789.3 and 804.0 eV [44,45]. The peak area ratios of Co³⁺/Co²⁺ in Ru-Co₃O₄ and Co₃O₄ were calculated to be 2.88 and 2.02, respectively, indicating that the electron density of Co sites in Ru-Co₃O₄ is obviously lower than that in Co₃O₄. Fig. 2c exhibits the O 1s XPS spectra of Ru-Co₃O₄ and Co₃O₄. Apart from the peaks corresponding to Co—O (529.3 eV) and Co—OH (530.5 eV) of Co₃O₄, the Ru-Co₃O₄ still possesses two additional peaks attributed to the Ru—O—Co (531.5 eV) and Ru—OH (532.5 eV) bonds, respectively [46,47]. Notably, the XPS peaks representing Co—O and Co—OH bonds in Ru-Co₃O₄ shift to the direction of lower binding energy compared to those in Co₃O₄, meaning the increased electron density on the O sites of Ru-Co₃O₄.

To further clarify the electronic structure and local coordination environment of catalysts, the X-ray absorption near-edge structure (XANES) and extended X-ray absorption fine structure (EXAFS) measurements were performed. As displayed in the Co K-edge XANES spectra (Fig. 2d), a positively shifted edge position for Ru-Co₃O₄ confirms the reduced electron density around the Co sites after Ru doping, which is consistent with the analysis of Co XPS spectra. Moreover, in the EXAFS spectra (Fig. 2e), the Co₃O₄ reference presents three typical characteristic peaks. The first major peak (1.52 Å) corresponds to the Co—O coordination in the first coordination shell, and the other two

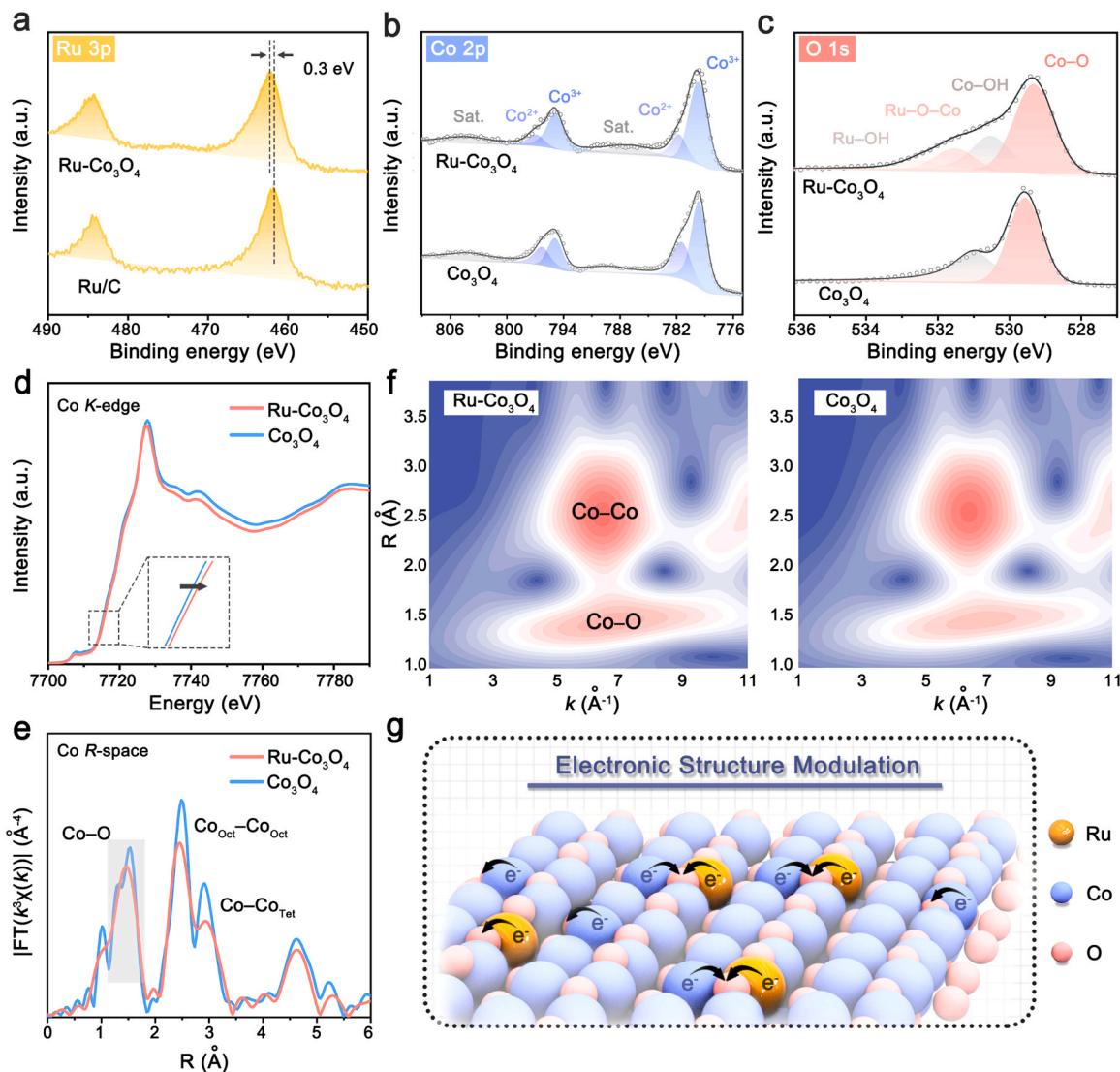


Fig. 2. (a) Ru 3p XPS spectra of Ru-Co₃O₄ and Ru/C. (b) Co 2p and (c) O 1s XPS spectra of Ru-Co₃O₄ and Co₃O₄. (d) Co K-edge XANES spectra, (e) EXAFS spectra, and (f) wavelet transform EXAFS contour plots of Ru-Co₃O₄ and Co₃O₄. (g) Schematic illustration of electronic structure modulation of embedded Ru—O—Co moieties.

peaks (2.49 and 2.91 Å) are originated from the nearest Co—Co coordination shell around octahedral Co site (Co_{Oct}—Co_{Oct}) and tetrahedral Co site (Co—Co_{Tet}), respectively [48]. Compared with Co₃O₄, a weaker peak intensity of all the bonds was found in Ru-Co₃O₄ and the peak positions representing Co—O and Co_{Oct}—Co_{Oct} shift to the lower R value region, indicating higher atomic chaos owing to the lattice distortion of Co₃O₄ induced by Ru doping [49]. Further wavelet transforms (WT) analysis shows that the Ru-Co₃O₄ only exhibits two strong WT signals corresponding to Co—O and Co—Co coordination of Co₃O₄, and the obvious signal from Co—Ru coordination is absent (Fig. 2f) [50]. This is probably due to the relatively low amount of doped Ru, which makes the Co—Ru signal difficult to detect. Therefore, based on the XPS, XANES, and EXAFS results, it can be inferred that the electron transfer from Ru and Co to O is realized in Ru-Co₃O₄, confirming the formation of embedded Ru—O—Co moieties with electron-deficient Co (Fig. 2g). More importantly, we found that the electronic structure modulation in the embedded Ru—O—Co moieties is different from that in the interfacial Ru—O—Co moieties of Ru@Co₃O₄ (Fig. S4). As seen in Fig. S5, the peak area ratio of Co²⁺/Co³⁺ in Ru@Co₃O₄ is larger than that corresponding to Co₃O₄ reference, reflecting higher electron density on Co of Ru@Co₃O₄. Furthermore, an obvious shift to the higher binding energy

direction was observed in the case of Ru@Co₃O₄ with respect to Ru/C, meaning the electron deficiency of Ru in Ru@Co₃O₄. These collective results suggest that the electrons are transferred from Ru to Co via bridged oxygen in Ru@Co₃O₄, thus forming the interfacial Ru—O—Co moieties with electron-rich Co. In comparison with the electron-rich Co in the interfacial Ru—O—Co moieties, the electron-deficient Co in the embedded moieties has an upshifted d-band center, which is favorable for enhancing the adsorption of reactant water molecules to trigger HER and oxygen-containing intermediates involved in OER [51]. Consequently, the unique electronic structure modulation of embedded Ru—O—Co moieties is reasonably believed to improve the HER/OER bifunctional performance.

3.2. HER/OER bifunctional catalytic performance

The HER performance of Ru-Co₃O₄ was first evaluated in 1 M KOH using a typical three-electrode configuration, where the catalyst loaded on carbon fiber paper was used as the working electrode, a saturated calomel electrode (SCE) as the reference electrode, and a graphite rod as the counter electrode (Fig. S6). As references, the catalytic performance of Co₃O₄, commercial Ru/C and Pt/C was also tested under the same

conditions. All measured potentials versus SCE were converted to potentials versus reversible hydrogen electrode (RHE) according to the Nernst equation ($E_{\text{RHE}} = E_{\text{SCE}} + 0.0592 \text{ pH} + 0.241$) [52]. The LSV curves reveal that the Ru-Co₃O₄ exhibits the best performance with the overpotential at 10 mA cm⁻² (η_{10}) of only 49 mV, which is significantly lower than that of Co₃O₄ (294 mV), and even surpasses that of Ru/C (81 mV) and Pt/C (62 mV) (Fig. 3a). The Tafel slope was employed to probe the reaction kinetics and the rate-determining step (RDS) of HER process. In general, different values of the Tafel slope manifest different reaction processes and RDS [53]. As displayed in Fig. 3c, the derived Tafel slopes of Ru-Co₃O₄, Co₃O₄, Ru/C, and Pt/C are approximately 46.2 mV dec⁻¹, 101.8 mV dec⁻¹, 63.4 mV dec⁻¹, and 43.2 mV dec⁻¹, respectively, suggesting that all these catalysts undergo the Volmer–Heyrovsky route [54]. Specifically, the RDS of Co₃O₄ is the Volmer step, while the RDS of other catalysts is the Heyrovsky step. It should be

noted that the Heyrovsky step also involves water dissociation, and thus the HER kinetics is still limited by the sluggish dissociation of water (Fig. S7) [53]. The reduced Tafel slope of Ru-Co₃O₄ indicates that the embedded Ru–O–Co moieties greatly promote the formation and dissociation of activated H₂O molecules, ultimately exhibiting a favourable reaction kinetics. Besides for Ru-based noble metal catalysts, the mass activity of Ru is essential and seriously affects the cost of catalyst [55]. Therefore, the apparent HER activity of Ru-Co₃O₄ was normalized according to the mass loading of Ru. The Ru-Co₃O₄ shows an impressive mass activity of 6.82 A mg⁻¹ at the HER overpotential of 130 mV, which is about an order of magnitude higher than that of both commercial Ru/C (0.66 A mg⁻¹) and Pt/C (0.67 A mg⁻¹). The mass activity of Ru-Co₃O₄ even substantially exceeds that of Ru@Co₃O₄ with interfacial Ru–O–Co moieties (1.11 A mg⁻¹), even though the Ru-Co₃O₄ and Ru@Co₃O₄ have similar nanosheet morphology and Ru

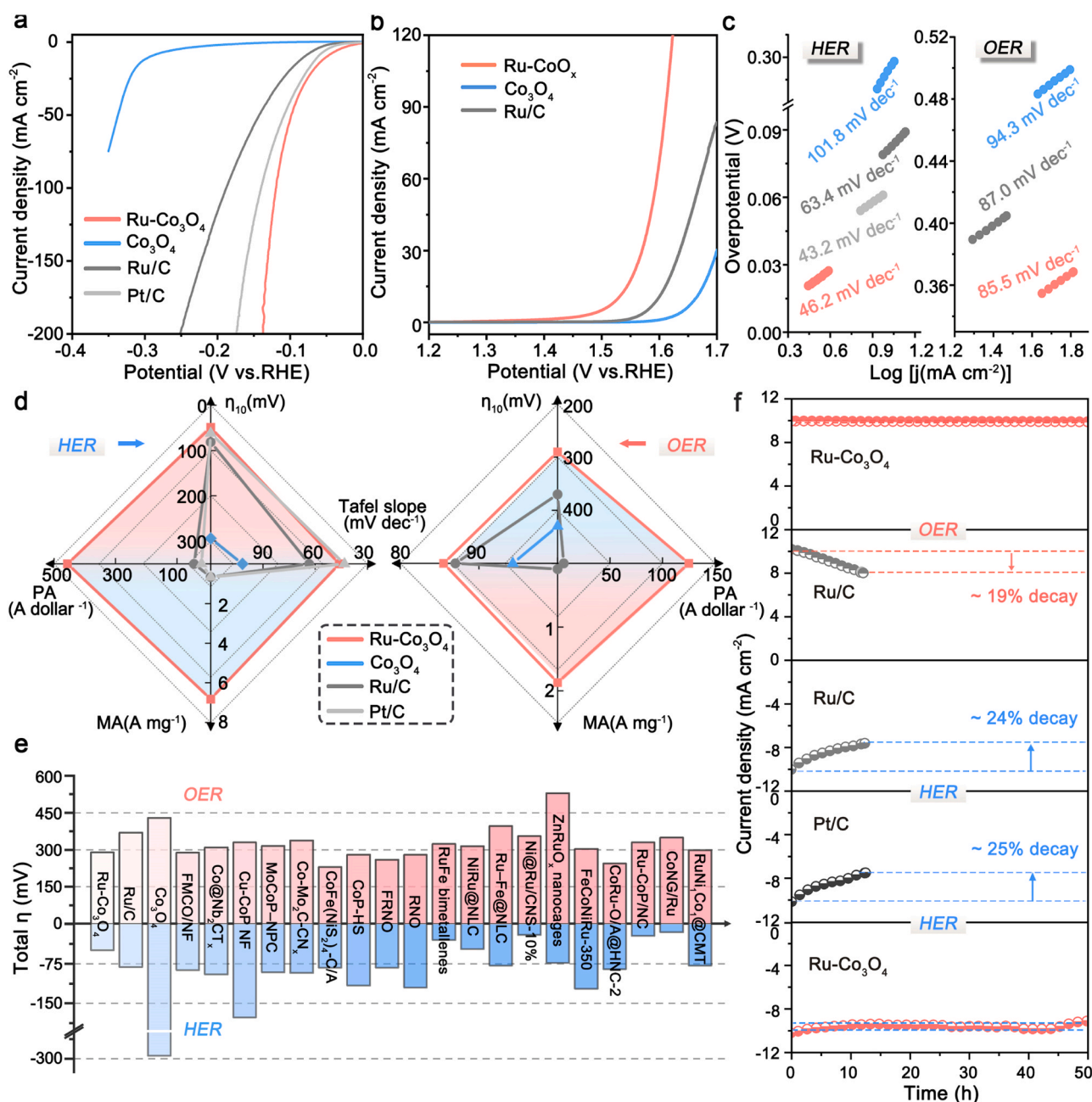


Fig. 3. (a) HER LSV curves of Ru-Co₃O₄, Co₃O₄, Ru/C, and Pt/C. (b) OER LSV curves of Ru-Co₃O₄, Co₃O₄, and Ru/C. (c) Corresponding Tafel plots. (d) The comparison of η_{10} , Tafel slope, MA, and PA among Ru-Co₃O₄, Co₃O₄, Ru/C, and Pt/C. (e) The comparison of the total overpotential of HER and OER between Ru-Co₃O₄ and the recently reported Ru-based, Co-based, and RuCo-based bifunctional catalysts. (f) Chronoamperometric curves for the Ru-Co₃O₄, Ru/C, and Pt/C.

content (Fig. S4 and S8, Table S1), signifying that the embedded Ru—O—Co structure is more advantageous than the interfacial structure for facilitating HER. The excellent mass activity of Ru-Co₃O₄ is attributed to the improved intrinsic activity and high site accessibility of embedded Ru—O—Co moieties. As presented in Fig. S9a, the TOF (the number of H₂ molecules produced per second from an active site) value of Ru-Co₃O₄ (27.9 H₂·s⁻¹) is about 1.85 times higher than that of Ru/C (15.1 H₂·s⁻¹), indicating a better intrinsic activity of Ru—O—Co moieties, meanwhile its C_{dl} (25.0 mF cm⁻²) increases by ~60% over Ru@Co₃O₄ (15.8 mF cm⁻²), meaning that the embedded Ru—O—Co in a few-layer structure is more beneficial for concentrating high-density accessible sites in contrast to the interfacial structure (Fig. S10 and Table S2). Impressively, the Ru-Co₃O₄ still exhibits the maximum HER price activity (normalized to price of Ru) of 456.19 A dollar⁻¹, which is 22.9, 10.3, and 6.1-fold greater than that of Pt/C (19.90 A dollar⁻¹), Ru/C (44.15 A dollar⁻¹), and Ru@Co₃O₄ (74.25 A dollar⁻¹), respectively, demonstrating that it is a cost-effective HER catalyst (Fig. 3d and S8b, Table S3). Fig. 3d more clearly shows the advantages of Ru-Co₃O₄ over other samples in these performance indicators, including η_{10} , Tafel slope, mass activity, and price activity. The EIS was carried out to study the electrical conductivity. The Ru-Co₃O₄ delivers a charge transfer resistance (R_{ct}) of only 36.8 Ω , much lower than that of Co₃O₄ and Ru/C, implying that the high-density Ru—O—Co moieties in few-layer structure greatly improve the interfacial electron transfer kinetics (Fig. S11 and Table S4).

In addition to catalytic activity, the stability of catalysts is another crucial criterion for evaluation. The Chronoamperometry response shows that the Ru-Co₃O₄ can keep the current density of 10 mA cm⁻² for 50 h, signifying its robust HER stability (Fig. 3f). This result is further supported by the LSV curve after long-term testing, which closely overlaps with the curve before testing (Fig. S12a). By contrast, the commercial Ru/C and Pt/C have a poor durability with a sharp activity decay of about 25% in 12 h. The post-HER Ru-Co₃O₄ was analyzed using SEM, XRD, Raman, and XPS characterizations, resulting in the observation that its morphology and composition were well-maintained (Fig. S13).

We also investigated the OER performance of the catalysts in the same alkaline environment. As presented in the LSV results (Fig. 3b), the Ru-Co₃O₄ exhibits a remarkably high OER activity, requiring an overpotential as low as 290 mV to achieve a current density of 10 mA cm⁻². This overpotential is much smaller than that of the benchmark Ru/C (370 mV) and Co₃O₄ (430 mV). Further analysis reveals that the Tafel slope of Ru-Co₃O₄ is only 85.5 mV dec⁻¹, in contrast with the values of Ru/C (87.0 mV dec⁻¹) and Co₃O₄ (94.3 mV dec⁻¹), suggesting a faster OER reaction kinetics. This result is reconfirmed by the EIS measurements, where the Ru-Co₃O₄ has the lowest R_{ct} value (Fig. S14 and Table S5). The OER mass activities and price activities of catalysts were compared in Fig. 3d. The Ru-Co₃O₄ catalyst displays an OER mass activity of 1.87 A mg⁻¹ and price activity of 125.08 A dollar⁻¹ at the overpotential of 350 mV, both of which are about 21.3 times higher than those of Ru/C (0.088 A mg⁻¹ and 5.89 A dollar⁻¹), and much superior to those of Ru@Co₃O₄ (1.11 A mg⁻¹ and 74.25 A dollar⁻¹) (Fig. S15). The outstanding mass activity and price activity of Ru-Co₃O₄ result from the obviously improved intrinsic activity of Ru—O—Co moieties and increased accessible site density (Fig. S9b and S16). Moreover, the Ru-Co₃O₄ catalyst exhibits highly enhanced OER durability compared to the commercial Ru/C. As shown in Fig. 3f and S12b, there is a negligible decrease of OER current density over a period of 50 h, and the polarization curve after the stability test almost coincides with the initial curve. Such an excellent HER/OER bifunctional catalytic performance of Ru-Co₃O₄ was further compared with that of Ru/C, Co₃O₄, and literature-reported results (Fig. 3e). The total overpotential of HER and OER for Ru-Co₃O₄ is merely 339 mV, which is substantially better than that for Ru/C (451 mV) and Co₃O₄ (724 mV), and even exceeds that for most reported Ru-based, Co-based, and RuCo-based catalysts (Table S6).

3.3. Performance improvement analysis of high-density accessible Ru—O—Co moieties

To figure out the root cause of the exceptional HER/OER bifunctional catalytic performance of Ru-Co₃O₄, the FTIR and in-situ Raman spectroscopy were conducted to monitor the adsorption of H₂O molecules in HER and the real-time change of key oxygen-containing species during the OER, respectively (Fig. 4a). Relative to the Ru/C, the Ru-Co₃O₄ presents a more obvious hydroxyl response signal at 2800–4000 cm⁻¹, indicating that the embedded Ru—O—Co moieties have a stronger H₂O adsorption ability and promote the formation of activated H₂O (Fig. 4c), as illustrated in Fig. S17 [14]. According to the previous study, the adsorption energy and dissociative kinetic barrier of H₂O follow a linear Brønsted–Evans–Polanyi (BEP) relationship [56]. Therefore, the strong H₂O adsorption capacity of embedded Ru—O—Co moieties in Ru-Co₃O₄ is beneficial for dissociating H₂O into H* for hydrogen production. This FTIR result is accordant with the HER Tafel slope, where the Ru-Co₃O₄ exhibits the fastest water dissociation step. Except for water adsorption/dissociation, the hydrogen adsorption is another key step affecting the cathodic HER. The calculation models and corresponding adsorption results are shown in Fig. S18 and S19. For the embedded Ru—O—Co moiety in Ru-Co₃O₄, the absolute value of hydrogen adsorption free energy ($|\Delta G_{H^*}|$) of Ru site (0.31 eV) is closer to zero than that of Co site (0.41 eV), which manifests that the Ru is the active center responsible for H* adsorption in the embedded moiety. This $|\Delta G_{H^*}|$ value is also smaller than that of Co₃O₄ (0.37 eV) and very close to that of pure Ru catalyst (0.18 eV), ensuring the feasible hydrogen adsorption and desorption (Fig. 4d). As a result, the suitable adsorption of water and H on the embedded Ru—O—Co moieties is responsible for excellent alkaline HER. Besides, the in-situ Raman results of Ru-Co₃O₄ and Ru/C are presented in Fig. 4b. The Ru-Co₃O₄ shows a typical peak at 693 cm⁻¹ corresponding to the stretching vibration of Co—O bonds in Co₃O₄, which is nearly unaffected with increase in applied bias [57]. Meanwhile, no other structural Raman signals from Co(OH)₂ and CoOOH are detected. Intriguingly, a new Raman peak belonging to Ru—O rather than Co—O bonds begins to emerge at about 817 cm⁻¹ when the anodic potential reaches 1.35 V, and its intensity increases first and then decreases with the potential rises (Fig. S20) [58]. As reported in the literature, the newly formed Raman peak in the wavenumber region of 800–1150 cm⁻¹ is assigned to the “active oxygen” species during OER [40]. Eventually when the potential sweeps to 1.60 V, the Raman peak from Ru—O bond completely disappears since the product oxygen shadows the signal (Fig. 4e). In contrast, the Ru/C starts to exhibit the Ru—O signal at the applied potential of 1.45 V, which is obviously higher than that of Ru-Co₃O₄, meanwhile the signal disappearance occurs much later. This phenomenon indicates the faster generation of “active oxygen” species for Ru-Co₃O₄ with embedded Ru—O—Co moieties, meaning the accelerated OER reaction rate. Based on the above water adsorption response and in-situ Raman, it can be concluded that the embedded Ru—O—Co moieties in the few-layer structure are favourable for the formation of key activated oxygen species during HER and OER catalysis, ultimately enhancing the HER/OER bifunctional performance.

3.4. Overall water/seawater splitting performance in an AEMWE

Overall water/seawater electrolysis performance is of high interest for practical applications, especially for those of bifunctional catalysts. Encouraged by the remarkable OER and HER activities of Ru-Co₃O₄, we evaluated its overall water/seawater splitting performance in an AEM electrolyzer (Fig. 5a and S21). The benchmark HER catalyst Pt/C and OER catalyst Ru/C were paired for comparison (Fig. S22). For overall water splitting, the electrolyzer consisting of Ru-Co₃O₄ requires extremely low cell voltages of 1.46 and 1.77 V to achieve 100 and 500 mA cm⁻² in 1 M KOH, which are significantly smaller than the Ru/C⁽⁺⁾||Pt/C⁽⁻⁾ pair electrolyzer (1.59 and 2.03 V). Surprisingly, this

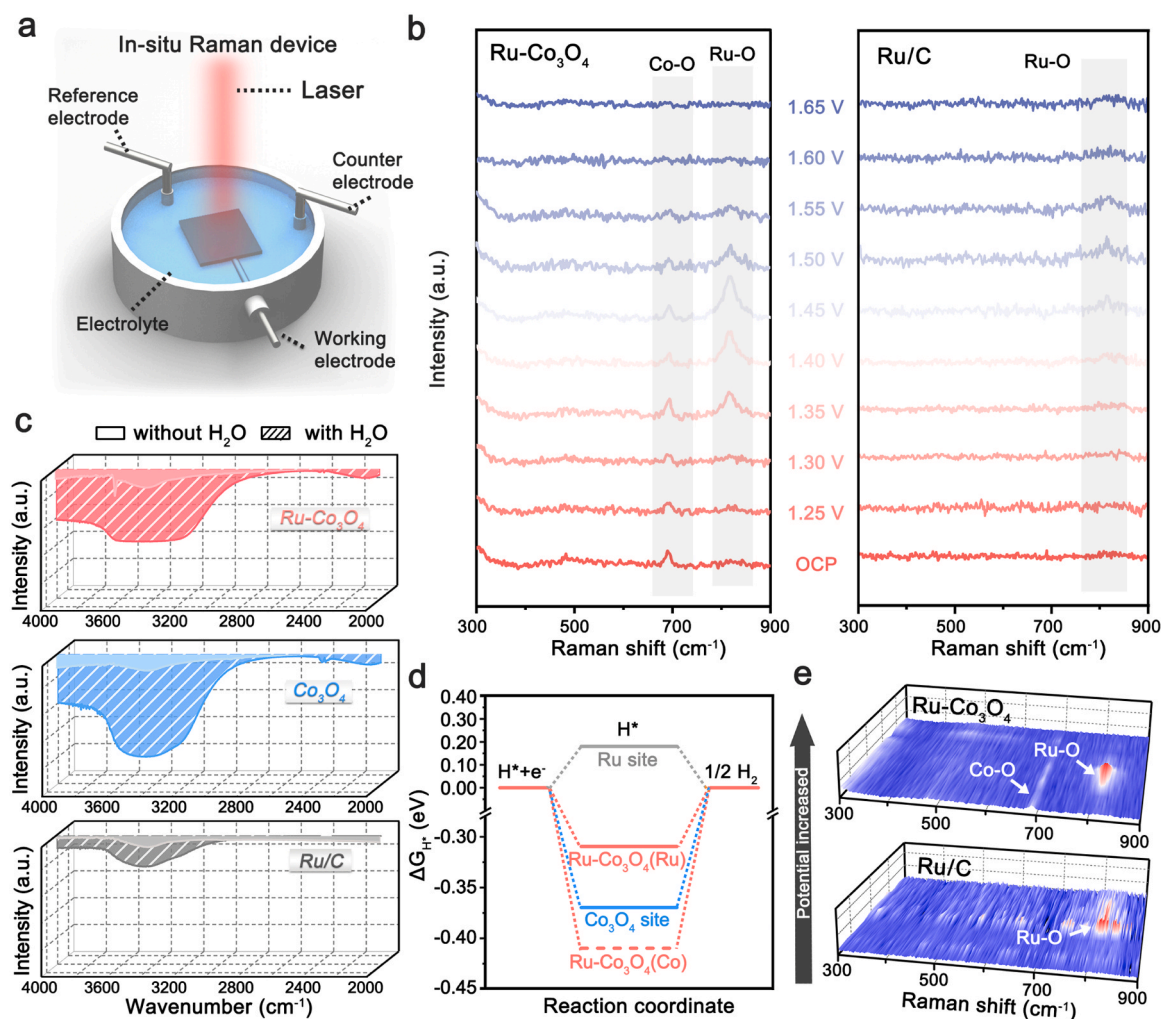


Fig. 4. (a) Setup diagram of the in-situ Raman device. (b) In-situ Raman and (e) corresponding 3D spectra of Ru-Co₃O₄ and Ru/C during the OER. (c) Water adsorption response and (d) the calculated ΔG_{H^+} values of Ru-Co₃O₄, Co₃O₄, and Ru/C.

electrolyzer can realize an ampere-level current density of 1 A cm^{-2} at the cell voltage of 2.03 V, about 2 times higher than that of the assembly of Ru/C and Pt/C ($\sim 0.5 \text{ A cm}^{-2}$) under the same condition, demonstrating the extraordinary catalytic activity of water electrolysis (Fig. 5b). The AEM electrolyzer was further applied for seawater splitting. In the presence of high-concentration Cl^- ions, the competing chlorine evolution reaction (CER) is the main side reaction hindering the selectivity of seawater electrolysis [59]. As the redox potential of OH^-/O_2 is lower than that of Cl^-/ClO^- in alkaline solution, OER is thermodynamically more advantageous than CER [60]. However, OER is a four-electron reaction that is kinetically unfavoured when compared with the two-electron CER. To be specific, the theoretical potential difference between CER and OER is 480 mV in an alkaline electrolyte, and thus CER can be thermodynamically suppressed as long as the potential is below 1.71 V [59]. Fig. 5c shows that at the cell voltage of 1.71 V, the electrolyzer assembled with Ru-Co₃O₄ can obtain an industrial-level current density of more than 400 mA cm^{-2} , whereas the current density of Ru/C⁽⁺⁾||Pt/C⁽⁻⁾ pair electrolyzer is only 173.3 mA cm^{-2} . The possible evolution of hypochlorite in the electrolyte was investigated using a colorimetric reagent after overall seawater splitting. As observed in Fig. S23, there is no color change in the reagent, indicating that no hypochlorite was formed during seawater electrolysis. We further compared the energy efficiency for hydrogen production of Ru-Co₃O₄ catalyst-assembled electrolyzer with the currently reported high-performance electrolyzers. Excitingly, the basic electricity expense

of our electrolyzer for water and seawater electrolysis is only 3.72 and $3.78 \text{ kWh m}^{-3} \text{ H}_2$ at the current density of 200 mA cm^{-2} , respectively, superior to the reported electrolyzers fabricated with Ru-based, Co-based, and RuCo-based bifunctional catalysts (Fig. 5e and Table S7). In addition, the durability of the as-assembled electrolyzer was also evaluated for overall water/seawater splitting. Fig. 5d reveals that there is no significant voltage degradation in the electrolyzer for 48 h continuous operation at 200 mA cm^{-2} in both alkaline freshwater and seawater electrolytes. The excellent overall water/seawater splitting performance of Ru-Co₃O₄ in AEM electrolyzer demonstrates the practical application ability.

4. Conclusions

In summary, the Ru was intentionally embedded into the few-layer Co₃O₄ nanosheets to construct high-density accessible Ru—O—Co moieties for alkaline freshwater and seawater electrolysis. This advanced catalyst architecture not only facilitates the formation and dissociation of activated H₂O molecules during the HER, but also ensures the fast generation of key “activated oxygen” species involved in OER, thereby significantly enhancing the HER/OER kinetics and bifunctional intrinsic activities, as evidenced with water adsorption response and in-situ Raman. Additionally, in comparison with the interfacial Ru—O—Co in Ru@Co₃O₄, the embedded moieties in the few-layer structure effectively promote the formation and accessibility of

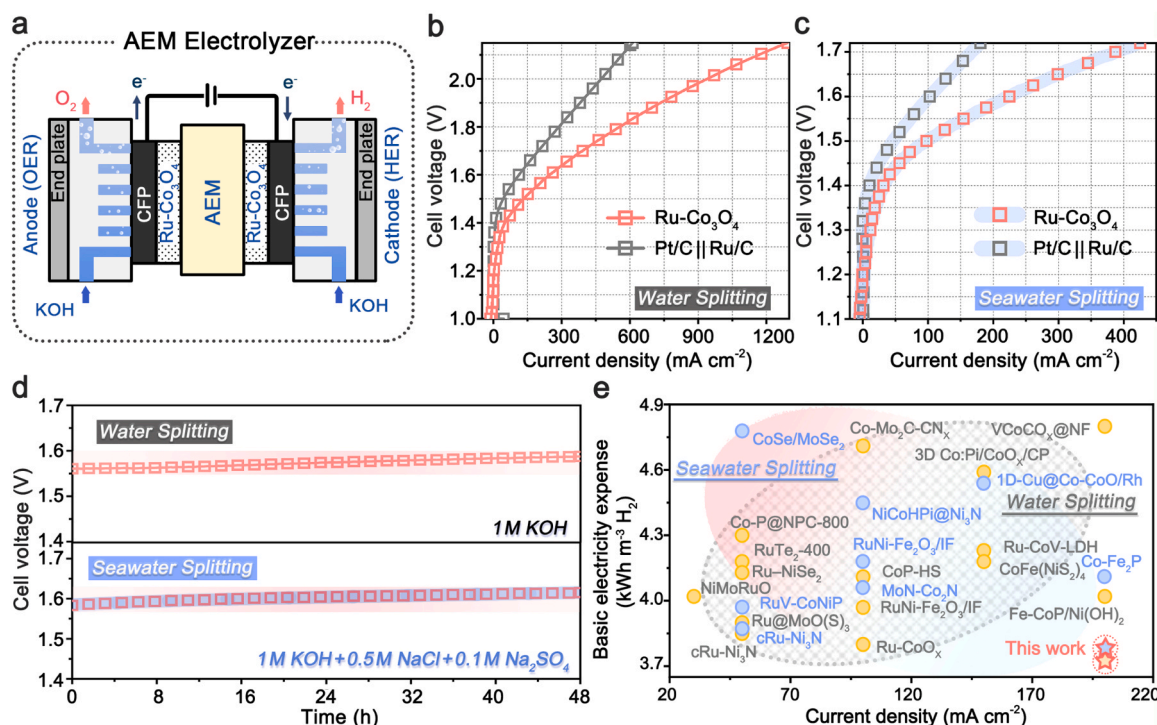


Fig. 5. (a) Schematic illustration of an AEM flow electrolyzer for water electrolysis. (b) Overall water splitting and (c) seawater splitting performance of Ru-Co₃O₄ and Pt/C||Ru/C. (d) Chronopotentiometry stability tests of Ru-Co₃O₄ for water and seawater electrolysis. (e) The performance comparison of our electrolyzer with the state-of-the-art water and seawater electrolyzers.

active sites. As an outcome, the Ru-Co₃O₄ catalyst with embedded Ru—O—Co achieves excellent HER/OER bifunctional performance, especially the mass activity and price activity. To be specific, the HER mass activity (6.82 A mg⁻¹) and price activity (456.19 A dollar⁻¹) of Ru-Co₃O₄ are more than one order of magnitude higher than those of Ru/C and Pt/C, and even its OER mass activity (1.87 A mg⁻¹) and price activity (125.08 A dollar⁻¹) reach 21.3 times than those of Ru/C. More impressively, when further applied in a practical AEM electrolyzer, the Ru-Co₃O₄ drives industrial-level current densities of 1 A cm⁻² at 2.03 V for water electrolysis and 0.41 A cm⁻² at 1.71 V for seawater electrolysis, more than twice than those of Ru/C⁽⁺⁾||Pt/C⁽⁻⁾ pair electrolyzer, while remaining a robust stability. Our work demonstrates that the design and construction of the embedded Ru—O—Co moieties in a few-layer structure is critical for boosting the mass activity and price activity of Ru catalyst in water/seawater splitting.

CRediT authorship contribution statement

Deqiang Kong: Investigation, Writing-original draft. **Chao Meng:** Research design, Writing-review & editing. **Yanmin Wang:** Formal analysis, Methodology, Investigation. **Xuemin Chen:** Methodology, Funding supporting. **Jialin Zhang:** Methodology, Investigation. **Lei Zhao:** Investigation, Visualization. **Jianglong Ji:** Investigation. **Liang Zhang:** Data curation. **Yue Zhou:** Conceptualization, Supervision, Writing-review & editing, Funding supporting.

Declaration of Competing Interest

The authors declare that they have no known competing financial interests or personal relationships that could have appeared to influence the work reported in this paper.

Data Availability

Data will be made available on request.

Acknowledgements

This work was supported by the National Natural Science Foundation of China (52301279, 51901115 and 51802075), the Shandong Provincial Natural Science Foundation, China (ZR2023MB122, ZR2019PEM001, and ZR2019BB009), and the Young Talents Program in University of Hebei Province, China (BJ2019002).

Appendix A. Supporting information

Supplementary data associated with this article can be found in the online version at [doi:10.1016/j.apcatb.2023.123578](https://doi.org/10.1016/j.apcatb.2023.123578).

References

- [1] L. Zeng, Z. Zhao, F. Lv, Z. Xia, S.-Y. Lu, J. Li, K. Sun, K. Wang, Y. Sun, Q. Huang, Y. Chen, Q. Zhang, L. Gu, G. Lu, S. Guo, Anti-dissolution Pt single site with Pt(OH)(O₃)/Co(P) coordination for efficient alkaline water splitting electrolyzer, *Nat. Commun.* 13 (2022) 3822.
- [2] X. Qin, B. Yan, D. Kim, Z. Teng, T. Chen, J. Choi, L. Xu, Y. Piao, Interfacial engineering and hydrophilic/aerophobic tuning of Sn₄P₃/Co₂P heterojunction nanoarrays for high-efficiency fully reversible water electrolysis, *Appl. Catal. B: Environ.* 304 (2022) 120923.
- [3] T. Meng, Y. Chen, D. Wang, L. Zhu, Y. Yan, Y. Yang, Z. Xing, X. Yang, Heteroatom inducing local geometrical configuration transformation of metallic oxygen clusters in metal hydroxide-organic frameworks with optimized hydrogen evolution performance, *Chem. Eng. J.* 468 (2023), 143707.
- [4] F.-L. Wang, Y.-W. Dong, C.-J. Yu, B. Dong, X.-Y. Zhang, R.-Y. Fan, J.-Y. Xie, Y.-N. Zhou, Y.-M. Chai, Trojan strategy assisted phase-pure Fe-NiCo₂S₄ for industrial anion-exchange membrane water electrolyzer, *Appl. Catal. B: Environ.* 331 (2023), 122660.
- [5] Y. Tan, J. Feng, H. Dong, L. Liu, S. Zhao, F. Lai, T. Liu, Y. Bai, I.P. Parkin, G. He, The edge effects boosting hydrogen evolution performance of platinum/transition bimetallic phosphide hybrid electrocatalysts, *Adv. Funct. Mater.* 33 (2023) 2209967.
- [6] L. Guo, J. Xie, S. Chen, Z. He, Y. Liu, C. Shi, R. Gao, L. Pan, Z.-F. Huang, X. Zhang, J.-J. Zou, Self-supported crystalline-amorphous composites of metal phosphate and NiS for high-performance water electrolysis under industrial conditions, *Appl. Catal. B: Environ.* 340 (2024), 123252.

- [7] Y. Zhou, Y. Wang, D. Kong, Q. Zhao, L. Zhao, J. Zhang, X. Chen, Y. Li, Y. Xu, C. Meng, Revealing the reactant mediation role of low-valence Mo for accelerated urea-assisted water splitting, *Adv. Funct. Mater.* 33 (2023) 2210656.
- [8] R.-Y. Fan, Y.-N. Zhou, M.-X. Li, J.-Y. Xie, W.-L. Yu, J.-Q. Chi, L. Wang, J.-F. Yu, Y.-M. Chai, B. Dong, In situ construction of Fe(Co)OOH through ultra-fast electrochemical activation as real catalytic species for enhanced water oxidation, *Chem. Eng. J.* 426 (2021), 131943.
- [9] K.-R. Yeo, K.-S. Lee, H. Kim, J. Lee, S.-K. Kim, A highly active and stable 3D dandelion spore-structured self-supporting Ir-based electrocatalyst for proton exchange membrane water electrolysis fabricated using structural reconstruction, *Energy Environ. Sci.* 15 (2022) 3449–3461.
- [10] Y.-N. Zhou, Y.-W. Dong, Y. Wu, B. Dong, H.-J. Liu, X.-J. Zhai, G.-Q. Han, D.-P. Liu, Y.-M. Chai, Nitrate induced precise atom substitution and vacancies for overall water splitting, *Chem. Eng. J.* 463 (2023), 142380.
- [11] J. Zhu, R. Lu, W. Shi, L. Gong, D. Chen, P. Wang, L. Chen, J. Wu, S. Mu, Y. Zhao, Epitaxially grown Ru clusters–nickel nitride heterostructure advances water electrolysis kinetics in alkaline and seawater media, *Energy Environ. Mater.* 6 (2023) 12318.
- [12] X. Liu, T. Wang, Y. Chen, J. Wang, W. Xie, R. Wu, X. Xu, L. Pang, X. Zhang, Y. Lv, G. Wang, Y. Yamauchi, T. Jin, Distinctive p-d orbital hybridization in RuSb nanobranched for simultaneously enhanced hydrogen evolution and hydrazine oxidation in alkaline seawater, *Appl. Catal. B: Environ.* 333 (2023), 122771.
- [13] S. Niu, X.-P. Kong, S. Li, Y. Zhang, J. Wu, W. Zhao, P. Xu, Low Ru loading RuO₂/(Co,Mn)₃O₄ nanocomposite with modulated electronic structure for efficient oxygen evolution reaction in acid, *Appl. Catal. B: Environ.* 297 (2021), 120442.
- [14] H. Li, K. Liu, J. Fu, K. Chen, K. Yang, Y. Lin, B. Yang, Q. Wang, H. Pan, Z. Cai, H. Li, M. Cao, J. Hu, Y.-R. Lu, T.-S. Chan, E. Cortés, A. Fratolocchi, M. Liu, Paired Ru–O–Mo ensemble for efficient and stable alkaline hydrogen evolution reaction, *Nano Energy* 82 (2021), 105767.
- [15] J. He, W. Li, P. Xu, J. Sun, Tuning electron correlations of RuO₂ by co-doping of Mo and Ce for boosting electrocatalytic water oxidation in acidic media, *Appl. Catal. B: Environ.* 298 (2021), 120528.
- [16] W. Wu, Y. Wu, D. Zheng, K. Wang, Z. Tang, Ni@Ru core-shell nanoparticles on flower-like carbon nanosheets for hydrogen evolution reaction at All-pH values, oxygen evolution reaction and overall water splitting in alkaline solution, *Electrochim. Acta* 320 (2019), 134568.
- [17] C. Cai, K. Liu, Y. Zhu, P. Li, Q. Wang, B. Liu, S. Chen, H. Li, L. Zhu, H. Li, J. Fu, Y. Chen, E. Pensa, J. Hu, Y.-R. Lu, T.-S. Chan, E. Cortés, M. Liu, Optimizing hydrogen binding on Ru sites with RuCo alloy nanosheets for efficient alkaline hydrogen evolution, *Angew. Chem. Int. Ed.* 61 (2022) 202113664.
- [18] Y. Yuan, W. Han, C. Zhang, Q. Sun, Y. Hao, J. Zhao, J. Zhao, X. Zhong, N. Zhang, An insight into the enhanced mechanism of Ru–MoO₂ interfacial chemical bonding for hydrogen evolution reaction in alkaline media, *Nano Res.* 16 (2023) 2230–2235.
- [19] T. Meng, Y. Chen, Z. Xing, X. Yang, Tuning phase structure of nickel–ruthenium alloys via MOFs in situ hydrolysis toward enhanced hydrogen evolution performance in alkaline, *Small Methods* 6 (2022) 2101188.
- [20] X. Liu, H. Qin, G. Wang, Q. Li, Q. Huang, Z. Wen, S. Mao, Co-doped Ni–Mo oxides: highly efficient and robust electrocatalysts for urea electrooxidation assisted hydrogen production, *J. Mater. Chem. A* 10 (2022) 16825–16833.
- [21] Y. Li, X. Zhou, W. Qi, H. Xie, K. Yin, Y. Tong, J. He, S. Gong, Z. Li, Ultrafast fabrication of Cu oxide micro/nano-structures via laser ablation to promote oxygen evolution reaction, *Chem. Eng. J.* 383 (2020), 123086.
- [22] X. Zhang, C. Feng, B. Dong, C. Liu, Y. Chai, High-voltage-enabled stable cobalt species deposition on MnO₂ for water oxidation in acid, *Adv. Mater.* 35 (2023) 2207066.
- [23] D. Wang, Y. Chen, L. Fan, T. Xiao, T. Meng, Z. Xing, X. Yang, Bulk and surface dual modification of nickel–cobalt spinel with ruthenium toward highly efficient overall water splitting, *Appl. Catal. B: Environ.* 305 (2022), 121081.
- [24] J. Li, Z. Liu, D.A. Cullen, W. Hu, J. Huang, L. Yao, Z. Peng, P. Liao, R. Wang, Distribution and valence state of Ru species on CeO₂ supports: support shape effect and its influence on CO oxidation, *ACS Catal.* 9 (2019) 11088–11103.
- [25] L.X. Chen, Z.W. Chen, M. Jiang, Z. Lu, C. Gao, G. Cai, C.V. Singh, Insights on the dual role of two-dimensional materials as catalysts and supports for energy and environmental catalysis, *J. Mater. Chem. A* 9 (2021) 2018–2042.
- [26] J. Xu, C. Chen, X. Kong, Ru–O–Cu center constructed by catalytic growth of Ru for efficient hydrogen evolution, *Nano Energy* 111 (2023), 108403.
- [27] D. Wang, D. Jiao, M. Gong, H. Fan, Y. Chen, L. Wang, J. Fan, J. Wu, D.J. Singh, J. Zhao, W. Zheng, X. Cui, Nickel metaphosphate supported ruthenium for all pH hydrogen evolution: from single atom, cluster to nanoparticle, *Appl. Catal. B: Environ.* 325 (2023), 122331.
- [28] H. Liu, G. Tan, M. Li, Z. Zhang, M. Getaye Sendeku, Y. Li, Y. Kuang, X. Sun, Single atomic ruthenium in WO₃ boosted hydrogen evolution stability at Ampere-level current density in whole pH range, *Chem. Eng. J.* 458 (2023), 141414.
- [29] Y. Zhou, C.-K. Dong, L.L. Han, J. Yang, X.-W. Du, Top-down preparation of active cobalt oxide catalyst, *ACS Catal.* 6 (2016) 6699–6703.
- [30] X. Du, Y. Ding, X. Zhang, Selectively Se-doped Co₃O₄@CeO₂ nanoparticle-dotted nanoneedle arrays for high-efficiency overall water splitting, *Appl. Surf. Sci.* 562 (2021), 150227.
- [31] R. Madhu, A. Karmakar, P. Arunachalam, J. Muthukumar, P. Gudlur, S. Kundu, Regulating the selective adsorption of OH[−] over the equatorial position of Co₃O₄ via doping of Ru ions for efficient water oxidation reaction, *J. Mater. Chem. A* 11 (2023) 21767–21779.
- [32] D. Hu, R. Wang, P. Du, G. Li, Y. Wang, D. Fan, X. Pan, Electrospinning Ru doped Co₃O₄ porous nanofibers as promising bifunctional catalysts for oxygen evolution and oxygen reduction reactions, *Ceram. Int.* 48 (2022) 6549–6555.
- [33] J. Niu, J. Yang, A.I. Channa, E. Ashalley, J. Yang, J. Jiang, H. Li, H. Ji, X. Niu, Enhancing the water splitting performance via decorating Co₃O₄ nanoarrays with ruthenium doping and phosphorization, *RSC Adv.* 10 (2020) 27235–27241.
- [34] C.-F. Li, L.-J. Xie, J.-W. Zhao, L.-F. Gu, H.-B. Tang, L. Zheng, G.-R. Li, Interfacial Fe–O–Ni–O–Fe bonding regulates the active Ni sites of Ni–MOFs via iron doping and decorating with FeOOH for super-efficient oxygen, *Evol., Angew. Chem. Int. Ed.* 61 (2022) 202116934.
- [35] Z. Cai, D. Zhou, M. Wang, S.-M. Bak, Y. Wu, Z. Wu, Y. Tian, X. Xiong, Y. Li, W. Liu, S. Siahrostami, Y. Kuang, X.-Q. Yang, H. Duan, Z. Feng, H. Wang, X. Sun, Introducing Fe²⁺ into nickel–iron layered double hydroxide: local structure modulated water oxidation activity, *Angew. Chem. Int. Ed.* 57 (2018) 9392–9396.
- [36] H. Liu, W. Shen, H. Jin, J. Xu, P. Xi, J. Dong, Y. Zheng, S.-Z. Qiao, High-performance alkaline seawater electrolysis with anomalous chloride promoted oxygen evolution reaction, *Angew. Chem. Int. Ed.* 62 (2023) 202311674.
- [37] G. Kresse, J. Furthmüller, Efficiency of ab-initio total energy calculations for metals and semiconductors using a plane-wave basis set, *Comput. Mater. Sci.* 6 (1996) 15–50.
- [38] J.P. Perdew, K. Burke, M. Ernzerhof, Generalized gradient approximation made simple, *Phys. Rev. Lett.* 77 (1996) 3865–3868.
- [39] S.-T. Xiao, R. Yin, L. Wu, S.-M. Wu, G. Tian, M. Shalom, L.-Y. Wang, Y.-T. Wang, F.-F. Pu, H.-N. Barad, F. Wang, X.-Y. Yang, Hierarchically porous few-layer carbon nitride and its high H⁺ selectivity for efficient photocatalytic seawater splitting, *Nano Lett.* 23 (2023) 4390–4398.
- [40] H.-Y. Wang, S.-F. Hung, Y.-Y. Hsu, L. Zhang, J. Miao, T.-S. Chan, Q. Xiong, B. Liu, In situ spectroscopic identification of μ -OO bridging on spinel Co₃O₄ water oxidation electrocatalyst, *J. Phys. Chem. Lett.* 7 (2016) 4847–4853.
- [41] L. Qiao, D. Liu, A. Zhu, J. Feng, P. Zhou, C. Liu, K.W. Ng, H. Pan, Nickel-facilitated in-situ surface reconstruction on spinel Co₃O₄ for enhanced electrochemical nitrate reduction to ammonia, *Appl. Catal. B: Environ.* 340 (2024), 123219.
- [42] R.-Y. Fan, H.-Y. Zhao, Y.-N. Zhen, F.-G. Wang, H. Hu, Y.-M. Chai, B. Dong, Mn-induced strengthening hybridization effect of Co–O bond for stable oxygen evolution in acidic media, *Fuel* 333 (2023), 126361.
- [43] J.A. Pratt, A.M. Shepherd, M.A. Hayward, Diamagnetic Ru²⁺ in Na₂La₂Ti₂RuO_{10–x} (0 < x < 2): a series of complex oxides prepared by topochemical reduction, *Inorg. Chem.* 54 (2015) 10993–10997.
- [44] J. Liu, H. Tang, P. Jian, B. Liu, Oxygen-vacancy defect engineering to boost the aerobic oxidation of limonene over Co₃O₄ nanocubes, *Appl. Catal. B: Environ.* 334 (2023), 122828.
- [45] Y. Li, L. Zhang, Z. Wang, L. Zhou, Y. Lan, C. Chen, Simultaneous oxidation of 4-aminophenylarsonic acid and adsorption of the produced inorganic arsenic by a combination of Co₃O₄–La₂CO₃@RSBC with peroxymonosulfate, *Chem. Eng. J.* 413 (2021), 127417.
- [46] P. Gao, Y. Zeng, P. Tang, Z. Wang, J. Yang, A. Hu, J. Liu, Understanding the synergistic effects and structural evolution of Co(OH)₂ and Co₃O₄ toward boosting electrochemical charge storage, *Adv. Funct. Mater.* 32 (2022) 2108644.
- [47] Q. Lu, Y. Guo, P. Mao, K. Liao, X. Zou, J. Dai, P. Tan, R. Ran, W. Zhou, M. Ni, Z. Shao, Rich atomic interfaces between sub-1 nm RuO_x clusters and porous Co₃O₄ nanosheets boost oxygen electrocatalysis bifunctionality for advanced Zn-air batteries, *Energy Storage Mater.* 32 (2020) 20–29.
- [48] Y. Lu, T. Liu, C.-L. Dong, Y.-C. Huang, Y. Li, J. Chen, Y. Zou, S. Wang, Tuning the selective adsorption site of biomass on Co₃O₄ by Ir single atoms for electrosynthesis, *Adv. Mater.* 33 (2021) 2007056.
- [49] S.-F. Hung, Y.-T. Chan, C.-C. Chang, M.-K. Tsai, Y.-F. Liao, N. Hiraoka, C.-S. Hsu, H. M. Chen, Identification of stabilizing high-valent active sites by operando high-energy resolution fluorescence-detected X-ray absorption spectroscopy for high-efficiency water oxidation, *J. Am. Chem. Soc.* 140 (2018) 17263–17270.
- [50] N. Han, S. Feng, Y. Liang, J. Wang, W. Zhang, X. Guo, Q. Ma, Q. Liu, W. Guo, Z. Zhou, S. Xie, K. Wan, Y. Jiang, A. Vlad, Y. Guo, E.M. Gaigneaux, C. Zhang, J. Fransaer, X. Zhang, Achieving efficient electrocatalytic oxygen evolution in acidic media on yttrium ruthenate pyrochlore through cobalt incorporation, *Adv. Funct. Mater.* 33 (2023) 2208399.
- [51] S. Jiao, X. Fu, H. Huang, Descriptors for the evaluation of electrocatalytic reactions: d-band theory and beyond, *Adv. Funct. Mater.* 32 (2022), 2107651.
- [52] C. Guan, X. Liu, W. Ren, X. Li, C. Cheng, J. Wang, Rational design of metal-organic framework derived hollow NiCo₂O₄ arrays for flexible supercapacitor and electrocatalysis, *Adv. Energy Mater.* 7 (2017) 1602391.
- [53] Q. Hu, K. Gao, X. Wang, H. Zheng, J. Cao, L. Mi, Q. Huo, H. Yang, J. Liu, C. He, Subnanometric Ru clusters with upshifted d band center improve performance for alkaline hydrogen evolution reaction, *Nat. Commun.* 13 (2022) 3958.
- [54] C. Yang, K. Shen, R. Zhao, H. Xiang, J. Wu, W. Zhong, Q. Zhang, X. Li, N. Yang, Balance effect: a universal strategy for transition metal carbides to enhance hydrogen evolution, *Adv. Funct. Mater.* 32 (2022) 2108167.
- [55] S. Zhou, H. Jang, Q. Qin, L. Hou, M.G. Kim, S. Liu, X. Liu, J. Cho, Boosting hydrogen evolution reaction by phase engineering and phosphorus doping on Ru/P-TiO₂, *Angew. Chem. Int. Ed.* 61 (2022) 202212196.
- [56] G. Lin, Z. Zhang, Q. Ju, T. Wu, C.U. Segre, W. Chen, H. Peng, H. Zhang, Q. Liu, Z. Liu, Y. Zhang, S. Kong, Y. Mao, W. Zhao, K. Suenaga, F. Huang, J. Wang, Bottom-up evolution of perovskite clusters into high-activity rhodium nanoparticles toward alkaline hydrogen evolution, *Nat. Commun.* 14 (2023) 280.
- [57] J. Zhang, W. He, T. Quast, J.R.C. Junqueira, S. Saddeler, S. Schulz, W. Schuhmann, Single-entity electrochemistry unveils dynamic transformation during tandem catalysis of Cu₂O and Co₃O₄ for converting NO₃[−] to NH₃, *Angew. Chem. Int. Ed.* 62 (2023) 202214830.

- [58] K.S. Joya, H.J.M. de Groot, Electrochemical in situ surface enhanced Raman spectroscopic characterization of a trinuclear ruthenium complex, Ru-red, *J. Raman Spectrosc.* 44 (2013) 1195–1199.
- [59] J. Guo, Y. Zheng, Z. Hu, C. Zheng, J. Mao, K. Du, M. Jaroniec, S.-Z. Qiao, T. Ling, Direct seawater electrolysis by adjusting the local reaction environment of a catalyst, *Nat. Energy* 8 (2023) 264–272.
- [60] M. Ning, F. Zhang, L. Wu, X. Xing, D. Wang, S. Song, Q. Zhou, L. Yu, J. Bao, S. Chen, Z. Ren, Boosting efficient alkaline fresh water and seawater electrolysis via electrochemical reconstruction, *Energy Environ. Sci.* 15 (2022) 3945–3957.